Chapter 7

Pressure driven iso-structural phase transition and its implication on the Néel skyrmion host hexagonal PtMnGa

In this chapter, we explore the pressure-dependent isostructural phase transition in the PtMnGa Néel skyrmion host system. We conducted experimental and simulation studies to assess the stability of skyrmions near or above room temperature.

7.1 Introduction

Magnetic skyrmions are topologically protected particlelike nanoscaled nontrivial spin textures that have been extensively studied in several systems [1–4], and it is gaining immense importance by virtue of their huge potential applications for low-power-consumption, ultradense storage and logic devices [5–8]. Since its discovery, magnetic skyrmions have been found in various magnetic materials and mainly studied in noncentrosymmetric materials, like MnSi [9–12], FeGe [13, 14], FeCoSi [15, 16], and Cu_2OSeO_3 [17–19] where the competing Heisenberg and Dzyaloshinskii-Moriya interaction (DMI) stabilized these nontrivial spin texture [20, 21]. Recently, it has also been discovered in centrosymmetric magnetic materials with uniaxial magnetic anisotropy, as reported in the Fe_3Sn_2 [22] and $La_{(2-2x)}Sr_{(1+2x)}Mn_2O_7$ [23], Gd_2PdSi_3 [24], $Gd_3Ru_4Al_{12}$ [25], $GdRu_2Si_2$ [26], $EuAl_4$ [27], MnPdGa [28]. In these centrosymmetric materials, the different topological magnetic spin textures can be stabilized by manipulating the helicity and vorticity [22]. The evolution and nature of magnetic spin texture are influenced by the various magnetic structures [29]. Due to the different symmetry of interaction between spin in the crystal lattice and the existence of a magnetic interface, magnetic skyrmions exhibit distinct spin dynamics. Depending on different directions of spin dynamics, magnetic skyrmions are classified into three types: Bloch [30], Néel [31], and antiskyrmions [2]. Néel-type skyrmions gained importance over other skyrmions because of their stability, dynamics and potential use in spin-based memory and logic devices [4]. In the Néel-type skyrmions, the magnetic moments rotate in the radial plane with the opposite-aligned moment at the periphery and core of the skyrmions [31]. Néel skyrmions have been observed with the broken inversion symmetry in nonmetallic compounds, e.g. GaV_4S_8 [31] and $VOSe_2O_5$ [32] and metallic systems like $Fe_3TeGe_2/Cr_2Te_2Ge_6$ [33], $Fe_3GeTe_2/[Co/Pd]_{10}$ [34].

PtMnGa is the first metallic system which shows the thermodynamically stable bulk type Néel skyrmions in the temperature range 210-220 K and weakly stable Néel skyrmions in a broad temperature range up to 5 K [35]. This compound shows paramagnetic (PM) behaviour at ambient temperature and switches to a ferromagnetic (FM) state at its Curie temperature ($T_C \sim 236$ K) [29]. Below T_C, it transforms to canted antiferromagnetic (CAFM) state at the temperature 175 K, followed by another transition from CAFM to the mixed CAFM and spin-density-wave state at 148 K [29]. These multiple magnetic transitions are due to the different strengths of magnetostructural coupling as evidenced by the temperature-dependent deviation observed in lattice parameters and volume magnetostriction [29]. A temperature-dependent abnormal change in the lattice parameters ratio has been reported at the maximum skyrmion density temperature, and crystal symmetry is preserved in the whole temperature range [36]. The abnormal change in the lattice parameters is directly related to isostructural phase transition [37, 38] or magnetoelastic coupling [39] The formation of stable skyrmions near room temperature is desirable for application in technological devices [40]. The stability of the skyrmionic phase is very sensitive to external stimuli like pressure, magnetic field, thermal annealing, ion irradiation, electric current etc. [3, 6, 40–45]. The application of pressure allows for studying and manipulating the properties of materials, leading to a better understanding of their behavior and the development of new materials with tailored characteristics [46]. Applying a small value of mechanical pressure can effectively change the crystal structure or the electronic configuration, leading to a change in the spin-lattice coupling and hence magnetic behaviour of the materials. The manipulation of the stability of skyrmions has been studied in MnSi [47], FeGe [48], and Cu_2OSeO_3 [49–51] systems using pressure. Recently, isostructural phase transition and shift in the maximum skyrmion density temperature has been studied in the MnNiGa magnet, which is the sister compound of PtMnGa, using pressure-dependent synchrotron X-ray powder diffraction (SXRPD) data analysis [52]. Interestingly, in the PtMnGa system, ferromagnetic transition temperature (T_C) increases with hydrostatic pressure with the rate of $dT_C/dP \sim 1.7$ K/kbar [53]. This suggests that there is a possibility to get the thermodynamically stable skyrmions temperature regime

(210-220 K) close to room temperature or even at a higher temperature, which necessitates a detailed pressure-dependent structural investigation of the PtMnGa system.

Here, we provide a detailed pressure-dependent structural study of the Néel skyrmions host PtMnGa system using SXRPD data. The Le Bail analysis of pressure-dependent SXRPD data shows a continuous contraction of unit-cell parameters (a and c, respectively). Across the whole pressure range, the crystal structure of PtMnGa remains hexagonal, and a departure from linear behaviour in the lattice parameters at about 6 GPa with pressure indicates an isostructural phase transition. Additionally, a second-order Birch-Murnaghan equation of state (B-M EoS) is used to fit the unit cell volume versus pressure curve, and it further confirms an isostructural phase transition occurs at pressures of $\sim$ 6GPa. Theoretical findings regarding magnetic moment, band structure, and density of states (DOS) with pressure concur with the experimental results. Our study demonstrates the pressure-induced isostructural phase transition in Néel skyrmions host PtMnGa.

7.2 Methods

A high-quality polycrystalline 4 g sample ingot of PtMnGa was prepared using standard arc melting furnace in an argon atmosphere, with a weight loss of approximately 0.07% [54–56]. To homogenise the sample, melting was done six times and followed by the annealing process for six days at 1073 K under the evacuated quartz, and then it was quenched under the ice-cold water. For the primary characterization, a small piece of the quenched bulk sample was ground into fine powder and then annealed in the vacuum condition to eliminate stress-induced effects originated during crushing [57–59]. X-ray powder diffraction measurement was done to check phase purity. Pressure-dependent SXRPD were performed at room temperature using high-energy (wavelength $\sim$ 0.4957 Å) collimated X-ray beam at XPRESS beamline Elettra, Trieste [60]. Typically, data were collected for an exposure time of 30 s at each pressure point, and several patterns were collected at close intervals up to 14.5 GPa pressure. 4:1 methanol–ethanol mixture was loaded as a pressure-transmitting medium inside a 100 μ m hole of a stainless steel gas-

ket. The pressure was independently measured by the ruby fluorescence method. A few ruby chips of diameter 5–8 μ m were loaded with the powder sample in the DAC pressure chamber to measure the pressure. The fit2D software integrates the collected two-dimensional (2D) image into one-dimensional (1D) (intensity vs 2θ) diffraction pattern. Magnetization measurement of zero field cooled sample was performed during heating at a low magnetic field of 100 Oe. The temperature-dependent low background and high-resolution SXRPD measurements were performed using high-flux (wavelength ~ 0.2071 Å) collimated X-ray beam at P02.1 beamline PETRA-III DESY, Hamburg, Germany. The temperature-dependent XRD data were measured isothermally. During the measurement, the temperature was ramped from the initial temperature to the next temperature, and then we waited an additional 2 minutes to ensure temperature stability before recording the diffraction pattern using the Perkin Elmer XRD1621 CN3 – EHS detector ($200 \times 200 \mu$ m^2 pixel size, 2048×2048 -pixel area). To corroborate the experimental findings, we have also performed the density functional theory calculations using the Quantum ESPRESSO (QE) software package. With the use of generalized gradient approximation (PBE-GGA) [61], the Kohn-Sham Hamiltonian is solved within the framework of pseudopotential (pp) and plane wave basis sets as implemented in QE [62]. Optimized norm-conserving Vanderbilt pseudopotential (ONCV pps) [63] are used in the calculations and the kinetic energy cutoff for the plane wave is taken as 80 Ry, which is sufficient for the norm-conserving pps. The electronic integration over the Brillouin zone is approximated by the Gaussian smearing of 0.01 Ry for the self-consistent (SC) calculations and tetrahedral occupation is considered for the DOS calculations. The Monkhorst-Pack k-grid of $8 \times 8 \times 6$ and $10 \times 10 \times 8$ are used for the SC and DOS calculations, respectively.

7.3 Results and discussion

7.3.1 Phase purity and phase transitions

To check the purity of the structural phase, we have performed room temperature SXRPD measurement. Figure 7.1 shows the Le Bail fit of room temperature SXRPD pattern. The calculated profile, as well as the observed pattern, are well matched, and each Bragg's

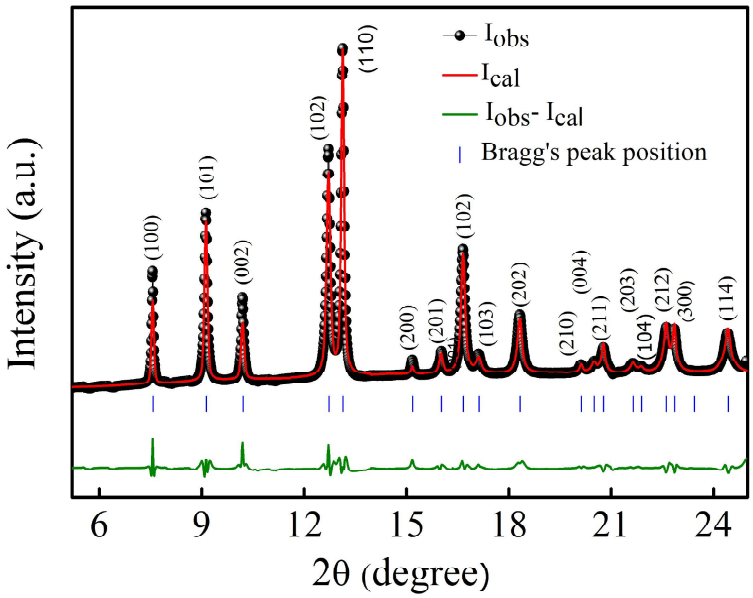

Figure 7.1: Le Bail fit of room temperature SXRPD pattern. Black dots, red and green solid lines, respectively, show the experimental data, calculated data and the residue. The blue ticks represent Bragg's peak positions.

peaks are well indexed using $P6_3/mmc$ space group, which confirms that PtMnGa crystallizes into the single-phase hexagonal structure as reported in the literature [64]. The room temperature lattice parameters ($a = b = 4.3319(5)$ Å, $c = 5.5832(8)$Å) were obtained using Le Bail refinement and well matched with the previous reports [29, 64]. To determine the magnetic phase transition, the temperature-dependence zero field cooled magnetization measurement was performed from 3 to 400 K under 100 Oe applied magnetic field (shown in Fig. 7.2) [65]. It shows a PM behavior at room temperature. As the temperature lowers below room temperature, there is a sudden change in the magnetization, reflecting the PM to FM ordering at its $T_C \sim 235$ K. Further lower down the temperature below T_C, there is a smooth and slight decrease in the magnetization below the ~ 220 K (inset of Fig. 7.2). In general, the magnetization increases with temperature as a function of $(T - T_C)^{1/2}$ at the PM to FM phase transition [66, 67], but this anomalous decrease in magnetization behaviour could be due to rearrangement of the FM spin structure into a non-trivial spin structure which favours thermodynamically stable skyrmions in the temperature range of 210 to 220 K. The decrease in magnetization is followed by a slope change at ~ 200 K, and the system transforms to a CAFM state. Further, with temperature decrease, it goes to mixed CAFM and spin density wave state at ~ 150 K.

These magnetic states and transition are highlighted with colour regimes in Fig. 7.2 and also well agreed with the literature [29]. Néel skyrmions are stable in the broad temperature regime from 5 to 220 K, but our focus of the study is on the temperature regime of 210 to 220 K due to its thermodynamic stability.

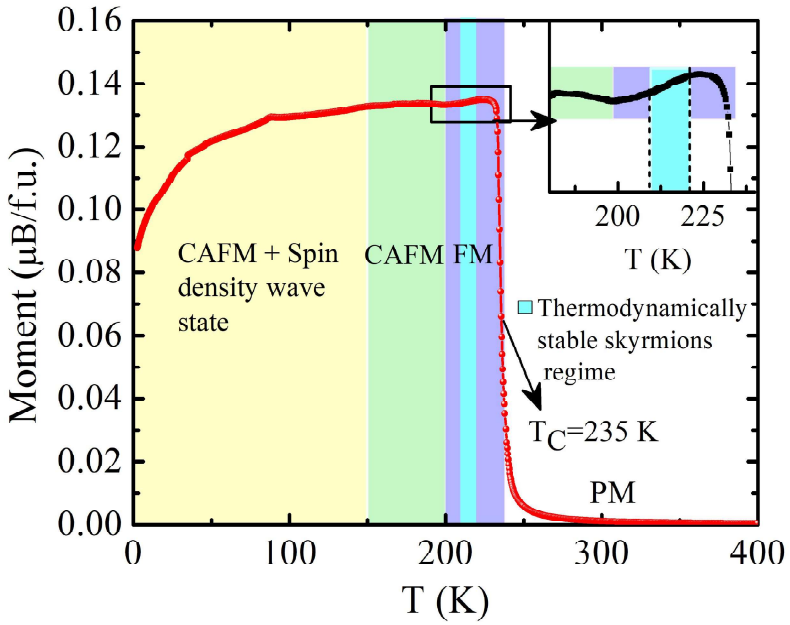

Figure 7.2: Zero field cooled magnetization measurement as a function of the temperature at low field (100 Oe) [65]. Magnetic states are highlighted with distinct colours. "T_C" represents the Curie temperature. Inset shows a magnified view of the plot around the thermodynamically stable skyrmions regime.

7.3.2 Pressure dependent structural analysis

Pressure-dependent SXRPD measurement was performed to study the crystal structure and phase transition under pressure conditions. In situ, pressure-dependent SXRPD measurement performed up to 14.5 GPa in the small steps of pressures at room temperature. Figure 7.3(a) displays the SXRPD patterns as a function of pressure. Peaks shift towards a larger 2θ angle as pressure rises, representing the compression of the unit cell characteristics. Across the pressure ramp, neither generation of new peaks nor the splitting in peaks denied the generation of a new structural phase with pressure. As pressure increases, the boarding in the peaks can be clearly observed from ambient pressure to high pressure. The applied pressure does cause increased stress, and this stress results in strained crys-

tallites in the system and results in broader peaks in SXRPD patterns. SXRPD patterns were also recorded during decompression to evaluate the structural behaviour with pressure release. A pattern is shown in Fig. 7.3(a) at 2.5 GPa during pressure release. The same number of peaks and positions demonstrate structural reversibility under pressure at room temperature. In contrast, other skyrmions host materials have also shown this irreversible tendency with pressure [49]. When pressure is applied to a material exhibiting a skyrmion phase, it can induce changes in the lattice parameters, interatomic distances, or magnetic interactions, impacting the stability and arrangement of skyrmion structures. The pressure-induced changes can sometimes lead to a reversible transformation between different skyrmion phases. PtMnGa system is more relevant than others since pressure has a negligible effect on its structure, and due to its reversible structural behaviour, it can be employed for pressure-tuned magnetic spin texturing devices. To study the compres-

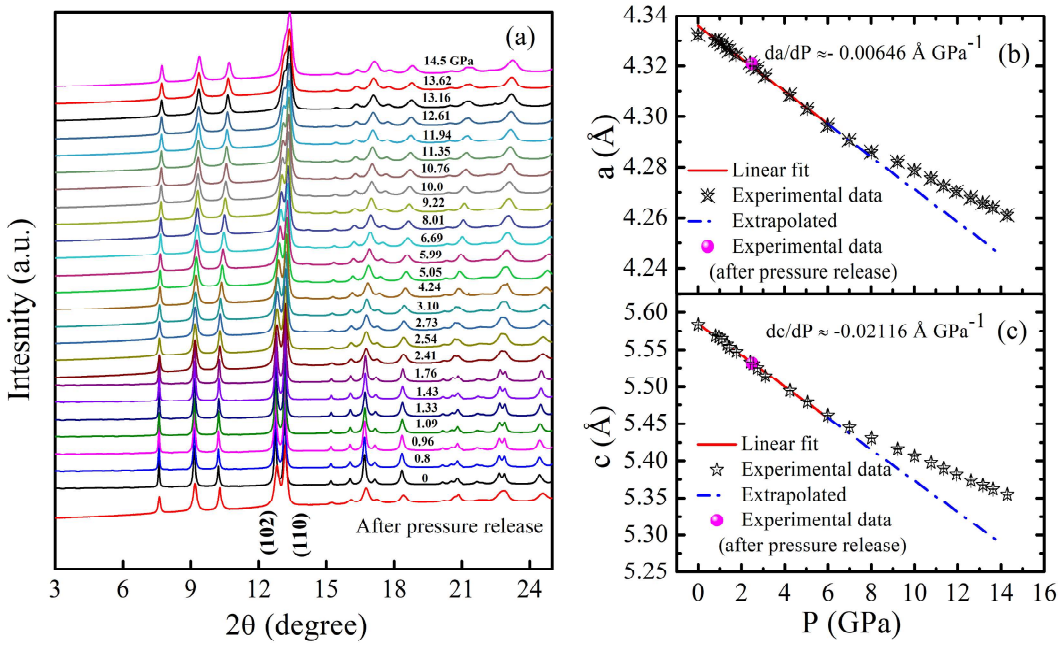

Figure 7.3: (a) Pressure-dependent SXRPD patterns with increasing pressure at room temperature. A pattern was also recorded during pressure release at 2.5 GPa. (b) Lattice parameters as a function of pressure along the a axis, i.e. in plane and (c) along the c axis, i.e. out of plane. The continuous red line represents the linear fitting, and the dotted blue line represents an extrapolated line, respectively. The slope of the line indicates the unit-cell parameter reduction rate with pressure. Magenta colour points correspond to the lattice parameter after pressure release at 2.5 GPa. The error in unit-cell parameters is smaller than the symbol size used for representation.

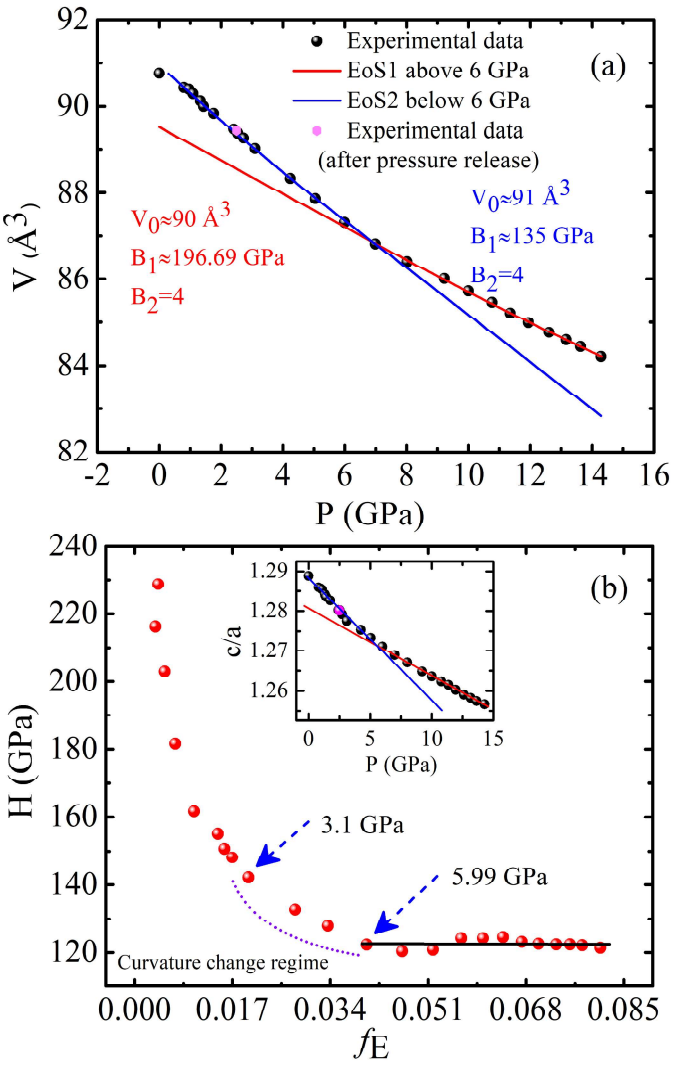

Figure 7.4: (a) Unit-cell volume as a function of pressure. Black dots represent the experimental data. Red and blue solid lines indicate the results of fitted data using B–M EoS above $\sim$ 6 GPa ("EoS1") and below the $\sim$6 GPa pressure ("EoS2") regime. A magenta colour point corresponds to the volume at 2.5 GPa after pressure release. (b) Reduced pressure (H) versus Eulerian strain (f_E) curve. Inset shows the c/a ratio as a function of pressure.

sion behaviour of the unit-cell parameters and structural phase transition with pressure, pressure-dependent unit-cell parameters are calculated from the Le Bail refinement (space group-$P6_3/mmc$) using pressure-dependent SXRPD data. Figures 7.3(b,c) depicts the pressure dependence of the unit-cell parameters. Unit-cell parameters change smoothly in low-pressure regimes up to 6 GPa. Linear fit up to 6 GPa shows linear compression behaviour of lattice parameters. The extrapolated linear fitted line, however, clearly differs from the linear behaviour above the 6 GPa pressure (Figs. 7.3(b,c)). Unit-cell parameters

decrease as the pressure rises with the rate $da/dP \sim -0.00646$ ÅGPa^{-1} (in ac plane) and $dc/dP \sim -0.02116$ ÅGPa^{-1} (perpendicular to ac plane), respectively. The compression behaviour of the lattice is not uniform in both (a and c) directions, which indicates the anisotropic compression of PtMnGa hexagonal lattice [52, 68]. After pressure release, the lattice parameter is also calculated at 2.5 GPa, which lies on the curve and shows the reversible nature of PtMnGa with pressure. Unit-cell volume (V) decreases with pressure since it is derived from the unit-cell characteristics (a and c), and a noticeable slope change can be seen in the unit-cell volume with the pressure below and above the 6 GPa pressure, as illustrated in Fig. 7.4(a). The inset of Fig. 7.4(b) shows a plot of the lattice parameter ratio (c/a) as a function of pressure. The larger negative slope and departure from the linear behaviour above 6 GPa are caused by the higher compression rate along the c axis. The distinct compression rates along the different crystallographic axes are usually found in the anisotropic crystals because of their weak van der Waals interaction [68]. As there is neither peak splitting nor the creation of additional peaks with pressure, the structural parameters (a and c), c/a, and V deviate from linearity above 6 GPa, indicating an isostructural phase transition [38, 68–73]. To further study of isostructural phase transition, a second-order B-M EoS [74, 75] was employed on the volume versus pressure curve. The B-M EoS is written as below:

$$P(V) = \frac{3B_1}{2}\left[\left(\frac{V_0}{V}\right)^{7/3} - \left(\frac{V_0}{V}\right)^{5/3}\right] \times \left[1 + \frac{3}{4}(B_2 - 4)\left[\left(\frac{V_0}{V}\right)^{2/3} - 1\right]\right] \quad (7.1)$$

Here, V is volume, V_0 reference volume, B_1 bulk modulus, and B_2 pressure derivative of bulk modulus [70]. The second-order B–M EoS can be derived by considering $B_2 = 4$ in the above equation [76, 77]. It is necessary to use two independent second-order B-M EoS for the two distinct regimes in the pressure versus volume curve because the data appears different in different pressure regimes, and considering the entire curve for fitting using a single EoS could not result in a better fit [78]. Figure 7.4(a) shows the result of fitting both the low-pressure (below 6 GPa) and high-pressure regimes (above 6 GPa). The value of the bulk modulus is ~ 135 GPa at the low-pressure regime and ~ 196 GPa at the high-pressure regime. However, in other skyrmions host materials, a large change in

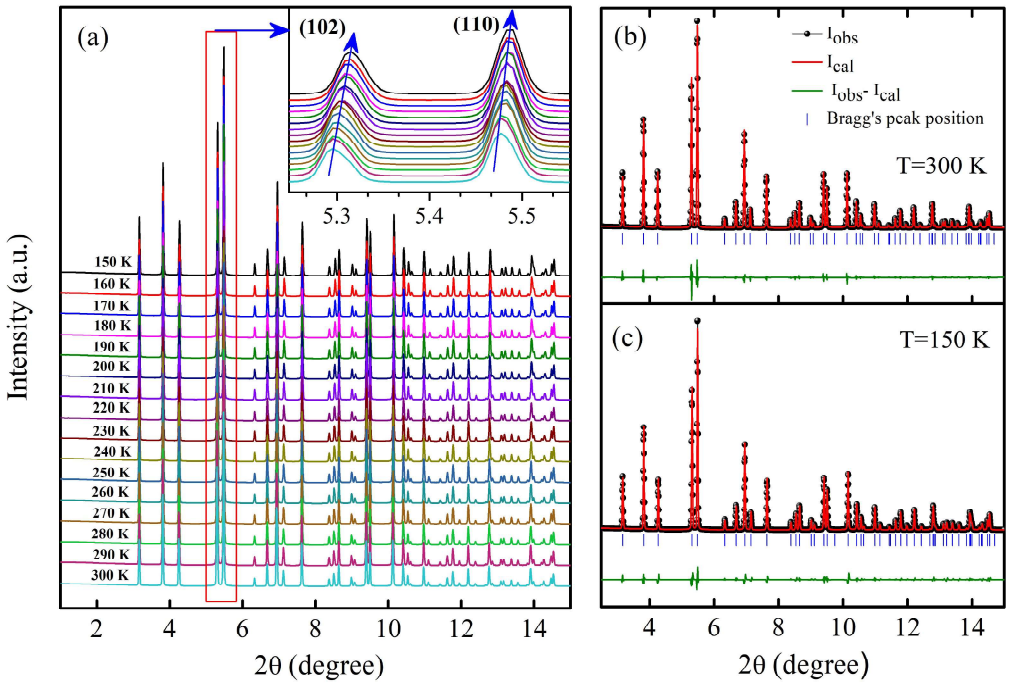

Figure 7.5: (a) The Evolution of SXRPD data as a function of the temperature from 150 to 300 K of PtMnGa system. Inset shows the magnified view of the peak shift around main Bragg's peak regime. (b) and (c) Le Bail fit of SXRPD data at 300 K [65] and 150 K, respectively. Black dots, red and green solid lines, respectively, show the experimental data, calculated data and the residue. The blue ticks represent Bragg's peak positions.

the bulk modulus has been observed with structural change [49]. So, a smaller change in Bulk modulus ($\sim$ 135 to $\sim$ 196 GPa) of PtMnGa evinces the isostructural phase transition above 6 GPa with pressure [52]. The larger value of the bulk modulus in the high-pressure regime displays lower compressibility in the high-pressure regime than the low-pressure regime [52, 70]. For a more accurate analysis of the experimental results, we performed the linearization of BM-EoS versus the Eulerian strain using Eq. 7.2 [79]:

$$H = B_1 + \frac{3B_1}{2}(B_2 - 4)f_E \tag{7.2}$$

H is the reduced pressure with $H = \frac{3P}{3f_E((1+2f_E))^{5/2}}$ and $f_E = \frac{1}{2}\left[\left(\frac{V_0}{V}\right)^2 - 1\right]$. The deviation of H from the linear behaviour indicates the presence of phase transition [80]. Figure 7.4(b) shows the H as a function of the f_E curve for the hexagonal PtMnGa system. As pressure increases, the curvature changes at about 3.1 GPa and becomes linear again at $\sim$ 5.99 GPa. The observed curvature of the H versus f_E plot from the linear behaviour

confirms the presence of phase transition in the present hexagonal PtMnGa, which confirms as isostructural phase transition ~ 6 GPa.

7.3.3 Temperature dependent structural analysis

To provide valuable insights into the structural behavior with temperature and explore the possibility of thermodynamically stable skyrmions regime to near room temperature, the temperature-dependent high-resolution SXRPD data of PtMnGa were measured. Temperature evolution of the SXRPD in the temperature range of 150 to 300 K is shown in Fig.

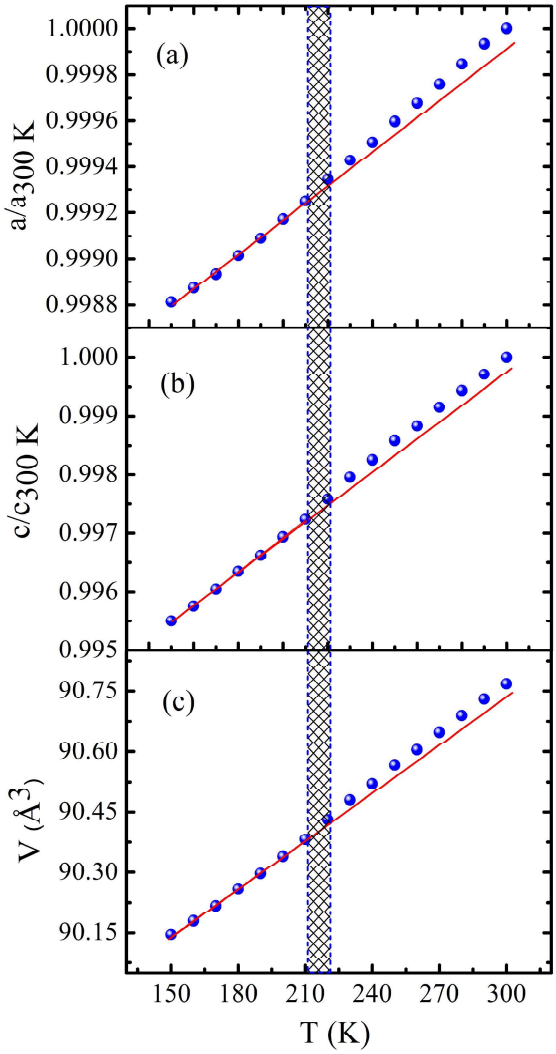

Figure 7.6: (a) $a/a_{300\ K}$ as a function of temperature along the a axis, i.e. in plane. (b) $c/c_{300\ K}$ as a function of temperature along the c axis, i.e. out of plane. (c) Volume as a function of temperature. The continuous red line represents the linear fitting. The error in unit-cell parameters is smaller than the symbol size used for representation.

7.5(a). Data is presented with the offset along the intensity axis for better representation. As usual, Bragg's peaks shift towards the higher 2θ with the decrease in temperature, as shown in the inset of Fig. 7.5(a). The absence of additional peaks and peak splitting with temperature suggest that the crystal symmetry of the PtMnGa system is maintained. Le Bail refinements of the temperature-dependent SXRPD patterns were performed with space group $P6_3/mmc$, suggesting that the hexagonal crystal structure of PtMnGa remains unchanged up to 300 K from 150 K. The fit of SXRPD patterns at the highest temperature (300 K) [65] and lowest (150 K) are shown in Figs. 7.5(b,c), respectively. The calculated in-plane and out of plane (a/a_{300K} and c/c_{300K}) lattice parameters and volume as a function of temperature are shown in Figs. 7.6(a-c), respectively. The lattice parameter increases with temperature in both the a and c directions. Lattice parameters and volume show deviation from linearity near the $\sim 210 - 220$ K, which is also a thermodynamically stable skyrmion regime and close to T_C where the magnetization starts decreasing at $\sim$ 220 K. FM T_C can be established at higher temperatures with pressure in PtMnGa system [53]. Comparison of the temperature-dependent (at ambient pressure) and pressure-dependent (at room temperature) unit cell volume results in that the unit cell volume at 210 K is approximately the same as the 0.8-1.09 GPa pressure. We conducted the micromagnetic simulations for 250 K under ambient (0 GPa) and at 0.6 GPa pressure. Our results showed that skyrmions, which were unstable at 0 GPa (at 250 K), became stable at 0.6 GPa pressure. This observation aligns with our experimental findings. This

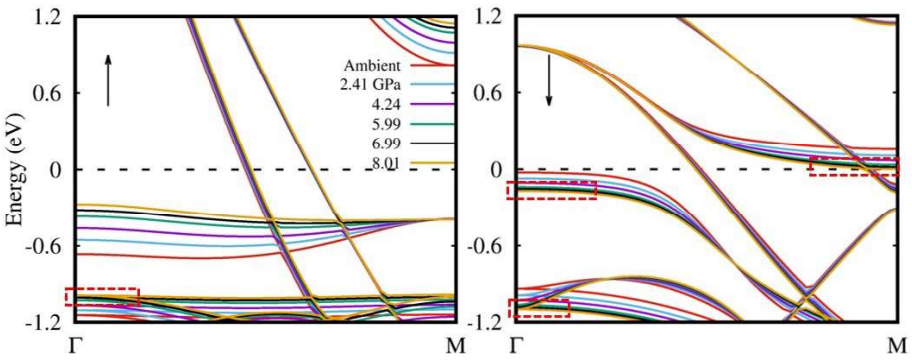

Figure 7.7: Electronic band structure at different representative pressures of the hexagonal PtMnGa in both the spin channels (majority and minority). The up and down arrows represent the spin majority and minority electrons, respectively. The regions where the red-coloured dotted rectangles highlight the degenerate bands.

concludes that thermodynamically stable Néel skyrmions can be moved to room temperature by using 0.8-1.09 GPa external pressure in the PtMnGa system. Similar to the above hydrostatic pressure (order of GPa), compressive/expansion pressure can also be attained chemically in a material. For example, when a thin film is deposited on a substrate, internal stress of the order of (GPa) is gained that mainly results from lattice mismatch or the substrate's thermal expansion [81–83] or doping an element into parent materials [84, 85]. So, with mechanical pressure, chemical pressure may also shift the thermodynamically stable skyrmion to room temperature. Doping a relatively smaller element in place of the Ga atom in the hexagonal PtMnGa system will create chemical pressure, which may cause the thermodynamically stable skyrmion to shift to room temperature, which requires more research. The presence of reversible isostructural phase transition with pressure in the Néel skyrmions host system is very important in pressure-tuned magnetic spin-texture device application.

7.3.4 Theoretical analysis of phase transition in PtMnGa

A substantial majority of materials that have the ability to host skyrmions undergo magnetostructural phase transitions. These transitions are critical as they adjust the symmetry and magnetic characteristics of a substance, potentially leading to the formation of a DMI, a foundational process for skyrmions' stabilization. Hence, from a theoretical standpoint, it becomes indispensable to examine the part played by magnetism, or more specifically, the magnetostructural coupling, in the isostructural phase transition in the hexagonal PtMnGa, a host of Néel skyrmions, which is driven by pressure as seen in the experiment. Therefore, our theoretical study is designed to explore the relationship between pressure, electronic structure, and magnetism. PtMnGa crystallizes in a hexagonal lattice, which exhibits various high-symmetry paths in the Brillouin zone of a Bravais lattice system. However, to facilitate comparison, we have specifically plotted the electronic bands along the Γ-M path (shown in Fig. 7.7). In the Brillouin zone, it is apparent that both spin majority and minority electrons exhibit degenerate eigenvalues at pressures equal to or greater than 6 GPa, as indicated by the red-colour dotted rectangles. This observation contrasts with the

behavior observed in NiMnGa, where the degeneracy was found below the crossover pressure [52]. One might argue that the observed degeneracy could be attributed to a small pressure difference of approximately 1 GPa (between 6 and 7 GPa, and 7 and 8 GPa). However, the degeneracy persists even when the pressure difference is 2 GPa (between 6 and 8 GPa). In contrast, below the crossover pressure, as depicted in Fig. 7.7, the eigenvalues at the marked regions are clearly nondegenerate for pressures of 2.41 and 4.24 GPa, despite the difference being less than 2 GPa (1.8 GPa). Hence, the theoretical results suggest that electrons in the lattice exhibit distinct behavior at pressures equal to or greater than 6 GPa compared to those below the crossover. We believe this discrepancy possibly

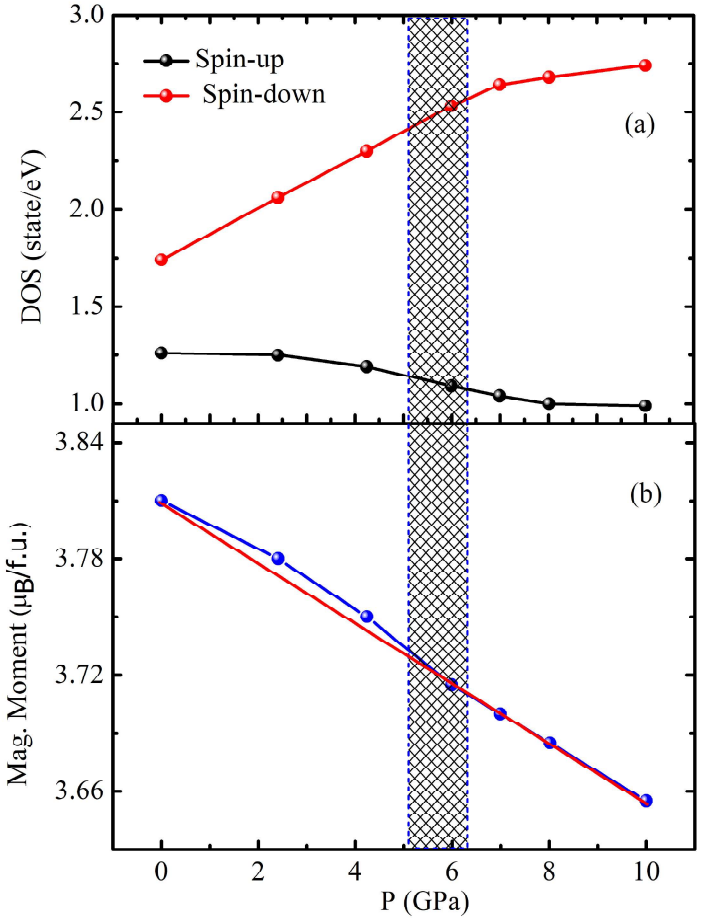

Figure 7.8: (a) The density of states at the Fermi level (Fermi energy set to zero) versus pressure curve for two spin channels. (b) shows the magnetic moment per formula unit. The red solid lines represent the linear fit.

plays a crucial role in the experimentally observed phase transition. To validate this, we performed spin-polarized density functional calculations, aiming for greater insights into

the electronic band structure, magnetic moment, and density of states (DOS) under varied pressure conditions. The role of the magneto-structural coupling can be understood as the density of states (DOS) in the minority electron channel changes rapidly up to 6 GPa, while the DOS in the majority electron case undergoes a smooth change (Fig. 7.8(a)). Above 6 GPa, the DOS at E_F is almost constant in both electron channels, which is a consequence of nearly the same E versus k dispersion above 6 GPa. The physical significance of this variation is that it indicates a change in the electronic structure (and magnetism) of the hexagonal PtMnGa system under pressure. The rapid change in the DOS of the minority electron channel up to 6 GPa suggests a change in the spin polarization of the electrons, which could be related to the observed phase transition, which is further understood from Fig. 7.8(b) where it shows magnetic moment slightly increases with the pressure initially and then decreases. The calculated magnetic moments at different pressures also reveal an interesting trend, indicating a phase transition at 6 GPa.

7.4 Comparison between isostructural transitions in MnNiGa and PtMnGa

PtMnGa and MnNiGa crystallize in the hexagonal structure from room temperature to the lower temperature (300 to 10 K). An anomaly in structural parameters with preserved crystallographic symmetry indicates the presence of isostructural phase transitions. A similar anomaly has been observed in lattice parameters of both MnNiGa and PtMnGa when subjected to pressure at room temperature. Therefore, MnNiGa and PtMnGa undergo isostructural transition at 4 GPa [52] and 6 GPa, respectively. These materials exhibit different compression rates along their a axis and c axis when subjected to the pressure. The differences in compression along these axes highlight that, although their overall structures are the same, their mechanical responses to pressure differ. In MnNiGa, it has been reported that the lattice parameters under the application of 0.7 GPa pressure at room temperature are close to the lattice parameters at the ambient pressure and $T \sim 200$K showing the maximum density of biskyrmions with the application of the magnetic field

[86], thus indicating the stabilization of the biskyrmions at room temperature by applying ~ 0.7 GPa pressure [52]. Accordingly, the observed pressure dependence of the unit cell volume at room temperature in PtMnGa may indicate the thermodynamically stable skyrmion regime at room temperature under a pressure of 0.8–1.09 GPa with the same cell volume as observed in the thermodynamically stable skyrmion regime around 210 K under ambient pressure. Despite their structural similarities and isostructural transition under pressure, MnNiGa and PtMnGa exhibit different types of skyrmion textures. PtMnGa displays Néel skyrmions, in which spins rotate in a radial plane as they move from the skyrmion core to the periphery, whereas MnNiGa exhibits biskyrmions, which are created by two skyrmions of opposite spin helicity. It is important to mention that the Néel skyrmions are known for the efficient motion under lower current densities, reduced skyrmion Hall effect, stability at room temperature etc [4, 87, 88]. Thus, both MnNiGa and PtMnGa systems undergo similar isostructural phase transitions, but exhibit distinct skyrmion textures, which causes different impacts in spintronics applications.

7.5 Pressure dependent magnetization measurement

Figure 7.9 presents the magnetization of the PtMnGa sample as a function of the magnetic field at 250 K, near T_C, under both ambient pressure (0.0 GPa) and 0.6 GPa pressure (the maximum pressure achievable during the experiment). The inset of Fig. 7.9 provides a zoomed view of the $M(H)$ curve at higher fields. As the pressure increases, the saturation magnetization also increases, indicating that the ferromagnetic properties are enhanced at higher pressure. Using this pressure-dependent data, we calculated the energy parameters, such as the magnetic anisotropy (K) and the exchange stiffness constant (A_{ex}). These parameters were then used to simulate the pressure-dependent skyrmions at 250 K using Object-Oriented Micromagnetic Framework (OOMMF) software [89].

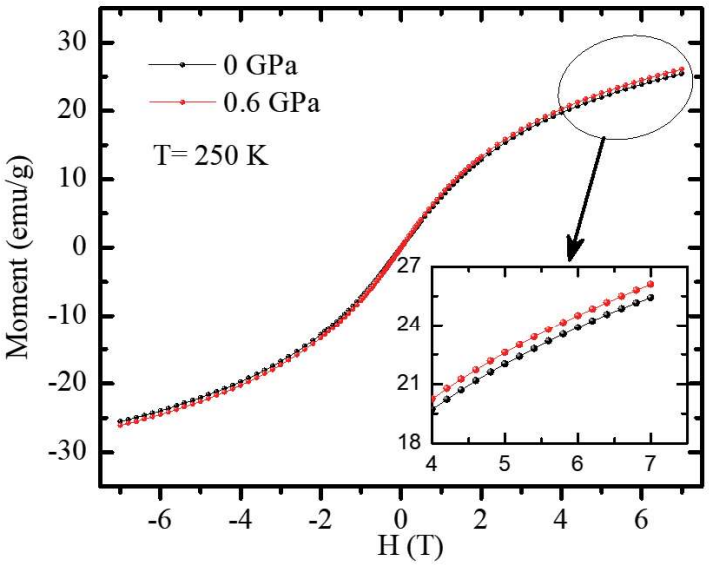

Figure 7.9: Field-dependent magnetization ($M(H)$) data of PtMnGa, measured at $T = 250$ K under 0 GPa and 0.6 GPa pressure. Inset shows the zoomed view of ($M(H)$) plot at higher field regime.

7.6 Calculation of magnetic anisotropy and exchange stiffness constant

We utilized the law of approach to saturation (LAS) method to determine the magnetic anisotropy [90]. In high-field regions, the relationship between magnetization (M) and the applied magnetic field (H) is typically described by LAS. The magnetic anisotropy constant (K) values, used to perform micromagnetic simulations, were obtained by fitting the experimental $M(H)$ data to the LAS model (Eq. 7.3 and Eq. 7.4) [90].

$$M = M_0 \left(1 - \frac{A}{H^2}\right) + \chi H \tag{7.3}$$

where M_0, χ, and A represent the spontaneous magnetization, high-field susceptibility, and a constant that depends on the magnetic anisotropy (K) and M_0 (Eq. 7.4), respectively.

$$A = \frac{4K^2}{15M_0^2} \tag{7.4}$$

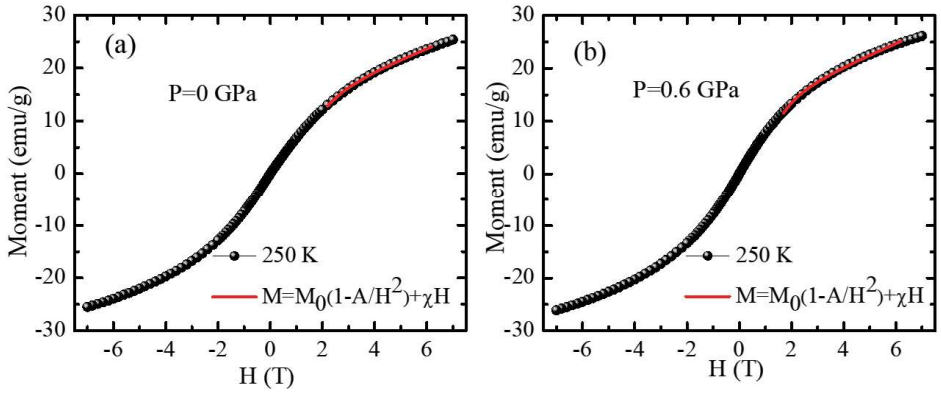

Figure 7.10: Fitting to the law of approach to saturation of [M(H)] data measured at 250 K (a) under 0 GPa pressure (b) 0.6 GPa pressure.

The calculated K values, derived from fitting the high-field region of the $M(H)$ curves, are 3.09×10^5 J/m^3 without pressure (0 GPa) and 2.48×10^5 J/m^3 under 0.6 GPa pressure at 250 K (Figs. 7.10(a,b)).

The value of A_{ex} is calculated by first deducing D through fitting the $T^{3/2}$ dependent $M_S(T)/M_S(0)$ data to the following equations [91, 92]:

$$\frac{M_S}{M_0} = 1 - BT^{3/2} \tag{7.5}$$

$$B = 2.612 \frac{g\mu_B}{M_S(0)} \left(\frac{k_B}{4\pi D} \right) \tag{7.6}$$

$$D = \frac{2A_{ex} g\mu_{\mathrm{B}}}{M_S} \tag{7.7}$$

where $M_S(T)$, $M_S(0)$, μ_B, g, and k_B represent the spontaneous magnetization at temperature T, the spontaneous magnetization at 0 K, the Bohr magneton, Lande's splitting factor, and the Boltzmann constant, respectively. The fitting shown in Fig. 7.11 gives the value of B from which we derived the values of the exchange stiffness constant (A_{ex}) using Eq. 7.4 and Eq. 7.5. The values of (A_{ex}) are calculated to be 1.2×10^{-12} J/m and 1.22×10^{-12} J/m at 250 K, without (0 GPa) and with pressure (0.6 GPa), respectively.

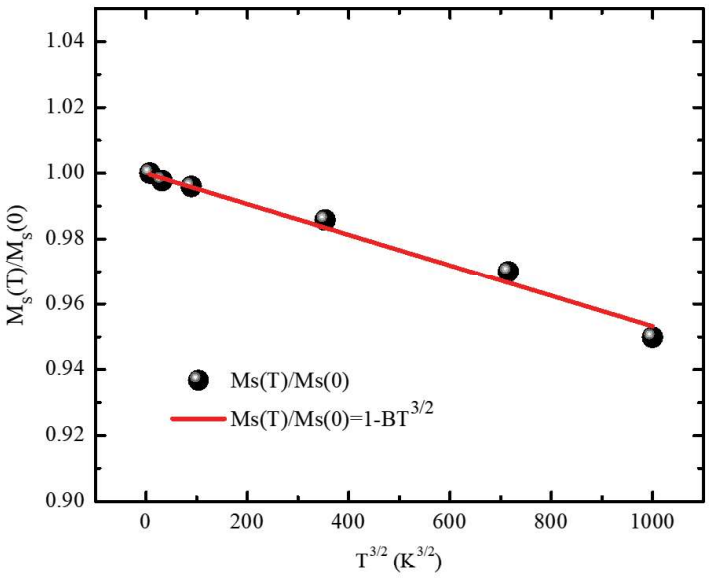

Figure 7.11: $M_S(T)/M_S(0)$ as a function of the $T^{(3/2)}$ and red line shows the fitted data at 7 T field.

7.7 Theory of micromagnetic simulation

To perform micromagnetic simulations, the magnetization dynamics are calculated by solving the time-dependent Landau-Lifshitz-Gilbert (LLG) equation [89, 93, 94]. The LLG equation is presented below [89].

$$\frac{dM}{dt} = -\mid \gamma \mid M \times H_{eff} + \frac{\alpha}{M_s}\left(M \times \frac{dM}{dt}\right) \tag{7.8}$$

where, M = magnetization ; M_s= Saturation magnetization ; H_{eff}= effective magnetic field; α =Phenomenological damping parameter, γ=Landau-Lifshitz gyromagnetic ratio. The H_{eff} is given by the following relation [95, 96]:

$$H_{eff} = -1/(\mu_0 M_S)(d\epsilon_{total}/dM). \tag{7.9}$$

Here, μ_0 represents permeability in vacuum, and ϵ_{total} is the system's total magnetic energy, which is given by Brown's equation [96–98]:

$$\epsilon_{total} = \int (\epsilon_{ex} + \epsilon_a + \epsilon_z + \epsilon_d + \epsilon_{DMI})\, dV \tag{7.10}$$

The terms ϵ_{ex}, ϵ_a, ϵ_z, ϵ_d, and ϵ_{DMI} represent exchange energy, anisotropy energy, Zeeman energy, demagnetization energy, and Dzyaloshinskii-Moriya interaction (DMI) energy, respectively. The OOMMF employs the finite difference method to solve the LLG equation. This approach necessitates dividing the sample into identical-volume parallelepipeds, referred to as cells. The OOMMF micromagnetic input format (.mif) includes input parameters and initial conditions for any given problem. Within each cell, physical properties such as total energy (ϵ_{tot}) and magnetization are calculated based on the specified energy parameters. Magnetization updates in each cell can be performed using two types of evolvers: the time evolver, which tracks the dynamics of the LLG equation, and the energy minimization evolver, which finds local energy minima through minimization techniques. The time evolver, specifically the 4^{th}-order Runge-Kutta evolver, solves the LLG equation as an ordinary differential equation over time. Control over these evolvers is managed by two drivers: the time driver for the time evolver and the minimization driver for the energy minimization evolver.

The topologically protected skyrmion is characterized by an integer known as the topological charge (Q) [1, 99].

$$Q = \frac{1}{4\pi} \int M \cdot (\partial_x M \times \partial_y M)\, dx\, dy, \tag{7.11}$$

where M is the unit vector in the direction of the magnetization.

7.8 Micromagnetic simulation and determination of topological charge

We conducted micromagnetic simulations for the present system at 0 and 0.6 GPa pressures and 250 K temperature (given in Fig. 7.12), using the OOMMF software to investigate the presence of skyrmionic structures [89]. The micromagnetic simulations are performed in the presence of local DMI induced by local symmetry breaking within a global centrosymmetric structure, utilizing the DMI extension module [65, 100]. The small value

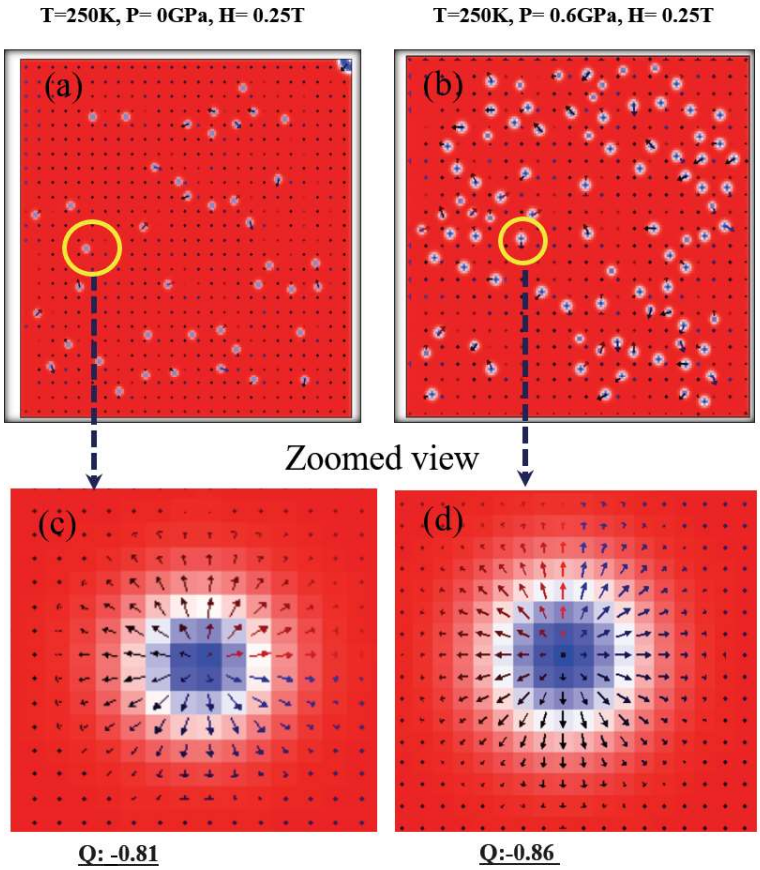

Figure 7.12: Micromagnetic simulation results for (a) 0 GPa, 250 K and 0.25 T (b) 0 GPa, 250 K and 0.25 T (c) and (d) calculation of topological charge.

of DMI of about 0.65 mJ/m^2 is taken as a local DMI [101, 102]. The simulations were conducted over an area of $300\times300\times2$ nm^3, divided into cells of $2\times2\times1$ nm^3. The simulation result at 0 GPa pressure is represented in Fig. 7.12(a), showing the non-coplanar spin structure, which is not the stable skyrmion, while multiple Néel skyrmions are found to be stabilized at 0.6 GPa pressure (at 0.25 T field), as shown in Fig. 7.12(b). As the magnetic field increases further, the field-polarized states start appearing (not shown here). The topological charge (Q) associated with the simulated skyrmion is calculated by using a Python library [103]. The calculated values of Q are -0.81 at 0 GPa pressure and -0.86 at 0.6 GPa pressure (Figs. 7.12(c,d)). Generally, the topological charge Q takes an integer charge only in a continuous and infinitely large system without a boundary. As present system has an underlying lattice structure and a finite size, the topological charge Q is not quantized, but the value of Q at 0.6 GPa pressure close to 1 (-0.86), which is acceptable with the boundary condition [104, 105]. This observation suggests that applying exter-

nal pressure can establish the skyrmions at higher temperatures, and a suitable pressure can shift the thermodynamically stable skyrmions regime to near room temperature in the PtMnGa system.

7.9 Comparison of lattice parameters at pressures with room temperature

A comparison of lattice parameters, where lattice parameters are calculated using temperature-dependent XRD (at ambient pressure) and pressure-dependent XRD (at room temperature), is shown in table 7.1. It can be seen from the table that the lattice parameters at 210 K (in thermodynamic stable skyrmions regime) are approximately the same as the lattice parameters at $\sim$ 1.09 GPa pressure. It suggests that the thermodynamically stable skyrmions regime can be moved to room temperature by application of the $\sim$ 1.09 GPa pressure.

Table 7.1: Comparison of temperature and pressure dependent lattice parameters (a and c) of hexagonal PtMnGa.

Temperature (K)	Lattice Parameters (Å)	Pressure (GPa)	Lattice Parameters (Å)
300	a=4.3321(5) c=5.5835(9)	ambient(0.0)	a=4.3329(4) c=5.5839(5)
250	a=4.3303(5) c=5.5770(8)	0.96	a=4.3300(2) c=5.5672(4)
210	a=4.3288(5) c= 5.5695(8)	1.09	a=4.3287(8) c=5.5643(4)
180	a=4.3278(2) c=5.5645(5)	1.33	a=4.3276(9) c=5.5571(6)

7.10 Conclusion

In conclusion, we performed the room-temperature pressure-dependent SXRPD on the Néel skyrmions host hexagonal PtMnGa system. The crystal structure remains preserved

in the whole applied pressure range (up to 14.5 GPa). Different linear compression rate of the in plane and out of plane lattice parameters was observed. The significant linear deviation in the lattice parameters and their ratio with pressure, along with consistent crystal symmetry (in the long-range order) across the entire pressure range, indicate an isostructural phase transition at approximately 6 GPa. Evidence for the isostructural phase transition is further confirmed by the implication of two distinct B-M EoS on the variation of the pressure-unit-cell volume curve. Theoretical calculations on band structure, magnetic moment, and density of states with pressure corroborate the experimental findings. We compared the pressure-dependent (at room temperature) with the temperature-dependent unit-cell volume (at ambient pressure). The unit-cell volume at 210 K (in the thermodynamically stable skyrmions regime) is nearly equal to that at 0.8-1.09 GPa pressure and room temperature. Our findings demonstrate the potential for pressure-tuning thermodynamically stable skyrmions near room temperature in the PtMnGa system. This suggests designing materials with stable skyrmions at higher temperatures and moderate pressures. The results provide a new pathway for future exploration of skyrmion stability through pressure tuning in similar systems. This work has significant implications for advancing the field of skyrmion research.

References

[1] A. Fert, N. Reyren, and V. Cros, "Magnetic skyrmions: advances in physics and potential applications," *Nat. Rev. Mater.*, vol. 2, no. 7, pp. 1–15, 2017.

[2] A. K. Nayak, V. Kumar, T. Ma, P. Werner, E. Pippel, R. Sahoo, F. Damay, U. K. Rößler, C. Felser, and S. S. P. Parkin, "Magnetic antiskyrmions above room temperature in tetragonal Heusler materials," *Nat.*, vol. 548, no. 7669, pp. 561–566, 2017.

[3] Y. Nii, T. Nakajima, A. Kikkawa, Y. Yamasaki, K. Ohishi, J. Suzuki, Y. Taguchi, T. Arima, Y. Tokura, and Y. Iwasa, "Uniaxial stress control of skyrmion phase," *Nat. Commun.*, vol. 6, no. 1, p. 8539, 2015.

[4] H. Y. Kwon, K. M. Song, J. Jeong, A.-Y. Lee, S.-Y. Park, J. Kim, C. Won, B.-C. Min, H. J. Chang, and J. W. Choi, "High-density Néel-type magnetic skyrmion phase stabilized at high temperature," *NPG Asia Mater.*, vol. 12, no. 1, p. 86, 2020.

[5] U. K. Roessler, A. Bogdanov, and C. Pfleiderer, "Spontaneous skyrmion ground states in magnetic metals," *Nat.*, vol. 442, no. 7104, pp. 797–801, 2006.

[6] X. Yu, N. Kanazawa, W. Zhang, T. Nagai, T. Hara, K. Kimoto, Y. Matsui, Y. Onose, and Y. Tokura, "Skyrmion flow near room temperature in an ultralow current density," *Nat. Commun.*, vol. 3, no. 1, p. 988, 2012.

[7] A. Fert, V. Cros, and J. Sampaio, "Skyrmions on the track," *Nat. Nanotechnol.*, vol. 8, no. 3, pp. 152–156, 2013.

[8] C. Felser and S. Parkin, "Topology, skyrmions, and Heusler compounds," *MRS Bull.*, vol. 47, no. 6, pp. 600–608, 2022.

[9] A. Neubauer, C. Pfleiderer, B. Binz, A. Rosch, R. Ritz, P. Niklowitz, and P. Böni, "Topological Hall effect in the phase of MnSi," *Phys. Rev. Lett.*, vol. 102, no. 18, p. 186602, 2009.

[10] S. Mühlbauer, B. Binz, F. Jonietz, C. Pfleiderer, A. Rosch, A. Neubauer, R. Georgii, and P. Böni, "Skyrmion lattice in a chiral magnet," *Sci.*, vol. 323, no. 5916, pp. 915–919, 2009.

[11] C. Pappas, E. Lelievre-Berna, P. Falus, P. Bentley, E. Moskvin, S. Grigoriev, P. Fouquet, and B. Farago, "Chiral paramagnetic skyrmion-like phase in MnSi," *Phys. Rev. Lett.*, vol. 102, no. 19, p. 197202, 2009.

[12] A. Tonomura, X. Yu, K. Yanagisawa, T. Matsuda, Y. Onose, N. Kanazawa, H. S. Park, and Y. Tokura, "Real-space observation of skyrmion lattice in helimagnet MnSi thin samples," *Nano Lett.*, vol. 12, no. 3, pp. 1673–1677, 2012.

[13] X. Yu, N. Kanazawa, Y. Onose, K. Kimoto, W. Zhang, S. Ishiwata, Y. Matsui, and Y. Tokura, "Near room-temperature formation of a skyrmion crystal in thin-films of the helimagnet FeGe," *Nat. Mater.*, vol. 10, no. 2, pp. 106–109, 2011.

[14] H. Wilhelm, M. Baenitz, M. Schmidt, U. Rößler, A. Leonov, and A. Bogdanov, "Precursor phenomena at the magnetic ordering of the cubic helimagnet FeGe," *Phys. Rev. Lett.*, vol. 107, no. 12, p. 127203, 2011.

[15] X. Yu, Y. Onose, N. Kanazawa, J. H. Park, J. Han, Y. Matsui, N. Nagaosa, and Y. Tokura, "Real-space observation of a two-dimensional skyrmion crystal," *Nat.*, vol. 465, no. 7300, pp. 901–904, 2010.

[16] W. Münzer, A. Neubauer, T. Adams, S. Mühlbauer, C. Franz, F. Jonietz, R. Georgii, P. Böni, B. Pedersen, M. Schmidt, *et al.*, "Skyrmion lattice in the doped semiconductor $Fe_{(1-x)}Co_xSi$," *Phys. Rev. B*, vol. 81, no. 4, p. 041203, 2010.

[17] Y. Onose, Y. Okamura, S. Seki, S. Ishiwata, and Y. Tokura, "Observation of magnetic excitations of skyrmion crystal in a helimagnetic insulator Cu_2OSeO_3," *Phys. Rev. Lett.*, vol. 109, no. 3, p. 037603, 2012.

[18] S. Seki, X. Yu, S. Ishiwata, and Y. Tokura, "Observation of skyrmions in a multiferroic material," *Sci.*, vol. 336, no. 6078, pp. 198–201, 2012.

[19] T. Adams, A. Chacon, M. Wagner, A. Bauer, G. Brandl, B. Pedersen, H. Berger,

P. Lemmens, and C. Pfleiderer, "Long-wavelength helimagnetic order and skyrmion lattice phase in Cu_2OSeO_3," *Phys. Rev. Lett.*, vol. 108, no. 23, p. 237204, 2012.

[20] I. Dzyaloshinsky, "A thermodynamic theory of "weak" ferromagnetism of antiferromagnetics," *J. Phys. Chem. Solids*, vol. 4, no. 4, pp. 241–255, 1958.

[21] T. Moriya, "Anisotropic superexchange interaction and weak ferromagnetism," *Phys. Rev.*, vol. 120, no. 1, p. 91, 1960.

[22] Z. Hou, W. Ren, B. Ding, G. Xu, Y. Wang, B. Yang, Q. Zhang, Y. Zhang, E. Liu, F. Xu, *et al.*, "Observation of various and spontaneous magnetic skyrmionic bubbles at room temperature in a frustrated kagome magnet with uniaxial magnetic anisotropy," *Adv. Mater.*, vol. 29, no. 29, p. 1701144, 2017.

[23] X. Yu, Y. Tokunaga, Y. Kaneko, W. Zhang, K. Kimoto, Y. Matsui, Y. Taguchi, and Y. Tokura, "Biskyrmion states and their current-driven motion in a layered manganite," *Nat. Commun.*, vol. 5, no. 1, p. 3198, 2014.

[24] T. Kurumaji, T. Nakajima, M. Hirschberger, A. Kikkawa, Y. Yamasaki, H. Sagayama, H. Nakao, Y. Taguchi, T.-h. Arima, and Y. Tokura, "Skyrmion lattice with a giant topological Hall effect in a frustrated triangular-lattice magnet," *Sci.*, vol. 365, no. 6456, pp. 914–918, 2019.

[25] M. Hirschberger, T. Nakajima, S. Gao, L. Peng, A. Kikkawa, T. Kurumaji, M. Kriener, Y. Yamasaki, H. Sagayama, H. Nakao, *et al.*, "Skyrmion phase and competing magnetic orders on a breathing kagomé lattice," *Nat. Commun.*, vol. 10, no. 1, p. 5831, 2019.

[26] N. D. Khanh, T. Nakajima, X. Yu, S. Gao, K. Shibata, M. Hirschberger, Y. Yamasaki, H. Sagayama, H. Nakao, L. Peng, *et al.*, "Nanometric square skyrmion lattice in a centrosymmetric tetragonal magnet," *Nat. Nanotechnol.*, vol. 15, no. 6, pp. 444–449, 2020.

[27] R. Takagi, N. Matsuyama, V. Ukleev, L. Yu, J. S. White, S. Francoual, J. R. Marde-

gan, S. Hayami, H. Saito, K. Kaneko, *et al.*, "Square and rhombic lattices of magnetic skyrmions in a centrosymmetric binary compound," *Nat. Commun.*, vol. 13, no. 1, p. 1472, 2022.

[28] X. Xiao, L. Peng, X. Zhao, Y. Zhang, Y. Dai, J. Guo, M. Tong, J. Li, B. Li, W. Liu, *et al.*, "Low-field formation of room-temperature biskyrmions in centrosymmetric MnPdGa magnet," *Appl. Phys. Lett.*, vol. 114, no. 14, 2019.

[29] J. A. Cooley, J. D. Bocarsly, E. C. Schueller, E. E. Levin, E. E. Rodriguez, A. Huq, S. H. Lapidus, S. D. Wilson, and R. Seshadri, "Evolution of noncollinear magnetism in magnetocaloric MnPtGa," *Phys. Rev. Mater.*, vol. 4, no. 4, p. 044405, 2020.

[30] N. Romming, C. Hanneken, M. Menzel, J. E. Bickel, B. Wolter, K. von Bergmann, A. Kubetzka, and R. Wiesendanger, "Writing and deleting single magnetic skyrmions," *Sci.*, vol. 341, no. 6146, pp. 636–639, 2013.

[31] I. Kézsmárki, S. Bordács, P. Milde, E. Neuber, L. M. Eng, J. S. White, H. M. Rønnow, C. Dewhurst, M. Mochizuki, K. Yanai, *et al.*, "Néel-type skyrmion lattice with confined orientation in the polar magnetic semiconductor GaV_4S_8," *Nat. Mater.*, vol. 14, no. 11, pp. 1116–1122, 2015.

[32] T. Kurumaji, T. Nakajima, V. Ukleev, A. Feoktystov, T.-h. Arima, K. Kakurai, and Y. Tokura, "Néel-type skyrmion lattice in the tetragonal polar magnet $VOSe_2O_5$," *Phys. Rev. Lett.*, vol. 119, no. 23, p. 237201, 2017.

[33] Y. Wu, B. Francisco, Z. Chen, W. Wang, Y. Zhang, C. Wan, X. Han, H. Chi, Y. Hou, A. Lodesani, *et al.*, "A van der waals interface hosting two groups of magnetic skyrmions," *Adv. Mater.*, vol. 34, no. 16, p. 2110583, 2022.

[34] M. Yang, Q. Li, R. Chopdekar, R. Dhall, J. Turner, J. Carlström, C. Ophus, C. Klewe, P. Shafer, A. N'Diaye, *et al.*, "Creation of skyrmions in van der waals ferromagnet Fe_3GeTe_2 on $(Co/Pd)_n$ superlattice," *Sci. Adv.*, vol. 6, no. 36, p. eabb5157, 2020.

[35] A. K. Srivastava, P. Devi, A. K. Sharma, T. Ma, H. Deniz, H. L. Meyerheim,

C. Felser, and S. S. Parkin, "Observation of robust Néel skyrmions in metallic PtMnGa," *Adv. Mater.*, vol. 32, no. 7, p. 1904327, 2020.

[36] G. Xu, Y. You, J. Tang, H. Zhang, H. Li, X. Miao, Y. Gong, Z. Hou, Z. Cheng, J. Wang, *et al.*, "Simultaneous tuning of magnetocrystalline anisotropy and spin reorientation transition via Cu substitution in Mn-Ni-Ga magnets for nanoscale biskyrmion formation," *Phys. Rev. B*, vol. 100, no. 5, p. 054416, 2019.

[37] D. Saha, R. Ranjan, D. Swain, C. Narayana, and T. N. G. Row, "An unusual temperature induced isostructural phase transition in a scheelite, $Li_{0.5}Ce_{0.5}MoO_4$," *Dalton Trans.*, vol. 42, no. 21, pp. 7672–7678, 2013.

[38] F. Occelli, D. L. Farber, J. Badro, C. M. Aracne, D. M. Teter, M. Hanfland, B. Canny, and B. Couzinet, "Experimental Evidence for a High-Pressure Isostructural Phase Transition in Osmium," *Phys. Rev. Lett.*, vol. 93, p. 095502, Aug 2004.

[39] A. Singh, A. Senyshyn, H. Fuess, T. Chatterji, and D. Pandey, "Neutron powder diffraction study of nuclear and magnetic structures of multiferroic $(Bi_{0.8}Ba_{0.2})(Fe_{0.8}Ti_{0.2})O_3$: Evidence for isostructural phase transition and magnetoelastic and magnetoelectric couplings," *Phys. Rev. B*, vol. 83, no. 5, p. 054406, 2011.

[40] X. Wang, A. Cao, S. Li, J. Tang, A. Du, H. Cheng, Y. Sun, H. Du, X. Zhang, and W. Zhao, "Manipulating density of magnetic skyrmions via multilayer repetition and thermal annealing," *Phys. Rev. B*, vol. 104, p. 064421, Aug 2021.

[41] A. Chacon, A. Bauer, T. Adams, F. Rucker, G. Brandl, R. Georgii, M. Garst, and C. Pfleiderer, "Uniaxial pressure dependence of magnetic order in MnSi," *Phys. Rev. Lett.*, vol. 115, no. 26, p. 267202, 2015.

[42] B. Ding, J. Cui, G. Xu, Z. Hou, H. Li, E. Liu, G. Wu, Y. Yao, and W. Wang, "Manipulating spin chirality of magnetic skyrmion bubbles by in-plane reversed magnetic

fields in $(Mn_{1-x}Ni_x)_{65}Ga_{35}$ (x= 0.45) magnet," *Phys. Rev. Appl.*, vol. 12, no. 5, p. 054060, 2019.

[43] Y. Hu, S. Zhang, Y. Zhu, C. Song, J. Huang, C. Liu, X. Meng, X. Deng, L. Zhu, C. Guan, *et al.*, "Precise Tuning of Skyrmion Density in a Controllable Manner by Ion Irradiation," *ACS Appl. Mater. Interfaces*, vol. 14, no. 29, pp. 34011–34019, 2022.

[44] B. Ding, X. Li, Z. Li, X. Xi, Y. Yao, and W. Wang, "Tuning the density of zero-field skyrmions and imaging the spin configuration in a two-dimensional Fe_3GeTe_2 magnet," *NPG Asia Mater.*, vol. 14, no. 1, p. 74, 2022.

[45] M. He, L. Peng, Z. Zhu, G. Li, J. Cai, J. Li, H. Wei, L. Gu, S. Wang, T. Zhao, *et al.*, "Realization of zero-field skyrmions with high-density via electromagnetic manipulation in Pt/Co/Ta multilayers," *Appl. Phys. Lett.*, vol. 111, no. 20, p. 202403, 2017.

[46] H.-K. Mao, B. Chen, J. Chen, K. Li, J.-F. Lin, W. Yang, and H. Zheng, "Recent advances in high-pressure science and technology," *Matter Radiat. at Extremes*, vol. 1, no. 1, pp. 59–75, 2016.

[47] L. J. Bannenberg, R. Sadykov, R. M. Dalgliesh, C. Goodway, D. L. Schlagel, T. A. Lograsso, P. Falus, E. Lelièvre-Berna, A. O. Leonov, and C. Pappas, "Skyrmions and spirals in MnSi under hydrostatic pressure," *Phys. Rev. B*, vol. 100, no. 5, p. 054447, 2019.

[48] K. Shibata, J. Iwasaki, N. Kanazawa, S. Aizawa, T. Tanigaki, M. Shirai, T. Nakajima, M. Kubota, M. Kawasaki, H. Park, *et al.*, "Large anisotropic deformation of skyrmions in strained crystal," *Nat. Nanotechnol.*, vol. 10, no. 7, pp. 589–592, 2015.

[49] S. Pal, P. Malavi, S. Chaturvedi, S. Das, S. Karmakar, D. Muthu, U. V. Waghmare, and A. Sood, "Tuning the structure of the skyrmion lattice system Cu_2OSeO_3 under pressure," *Phys. Rev. B*, vol. 102, no. 21, p. 214107, 2020.

[50] I. Levatić, P. Popčević, V. Šurija, A. Kruchkov, H. Berger, A. Magrez, J. White, H. M. Rønnow, and I. Živković, "Dramatic pressure-driven enhancement of bulk skyrmion stability," *Sci. Rep.*, vol. 6, no. 1, p. 21347, 2016.

[51] L. Deng, H.-C. Wu, A. P. Litvinchuk, N. F. Yuan, J.-J. Lee, R. Dahal, H. Berger, H.-D. Yang, and C.-W. Chu, "Room-temperature skyrmion phase in bulk Cu_2OSeO_3 under high pressures," *Proc. Natl. Acad. Sci.*, vol. 117, no. 16, pp. 8783–8787, 2020.

[52] A. K. Singh, P. Devi, A. K. Jena, U. Modanwal, S.-C. Lee, S. Bhattacharjee, B. Joseph, and S. Singh, "Pressure-Induced Isostructural Phase Transition in Biskyrmion Host Hexagonal MnNiGa," *Phys. Status Solidi Rapid Res. Lett.*, vol. 16, no. 7, p. 2200057, 2022.

[53] T. Kanomata, K. Shirakawa, and T. Kaneko, "Effect of hydrostatic pressure on the curie temperature of the hexagonal compound PtMnGa," *Phys. Stat. Sol. (a)*, vol. 97, no. 2, pp. K149–K152, 1986.

[54] F.-X. Hu, B.-g. Shen, and J.-r. Sun, "Magnetic entropy change in $Ni_{51.5}Mn_{22.7}Ga_{25.8}$ alloy," *Appl. Phys. Lett.*, vol. 76, no. 23, pp. 3460–3462, 2000.

[55] S. Singh, L. Caron, S. W. D'Souza, T. Fichtner, G. Porcari, S. Fabbrici, C. Shekhar, S. Chadov, M. Solzi, and C. Felser, "Large Magnetization and Reversible Magnetocaloric Effect at the Second-Order Magnetic Transition in Heusler Materials," *Adv. Mater.*, vol. 28, no. 17, pp. 3321–3325, 2016.

[56] S. Singh, R. Rawat, and S. Barman, "Existence of modulated structure and negative magnetoresistance in ga excess Ni−Mn−Ga," *Appl. Phys. Lett.*, vol. 99, no. 2, p. 021902, 2011.

[57] W. H. Wang, Z. H. Liu, J. Zhang, J. L. Chen, G. H. Wu, W. S. Zhan, T. S. Chin, G. H. Wen, and X. X. Zhang, "Thermoelastic intermartensitic transformation and its internal stress dependency in $Ni_{52}Mn_{24}Ga_{24}$ single crystals," *Phys. Rev. B*, vol. 66, p. 052411, Aug 2002.

[58] S. Singh, P. Kushwaha, F. Scheibel, H.-P. Liermann, S. Barman, M. Acet, C. Felser, and D. Pandey, "Residual stress induced stabilization of martensite phase and its effect on the magnetostructural transition in Mn-rich Ni – Mn – In/Ga magnetic shape-memory alloys," *Phys. Rev. B*, vol. 92, no. 2, p. 020105, 2015.

[59] R. Ranjan, S. Singh, H. Boysen, D. Trots, S. Banik, A. Awasthi, P. Mukhopadhyay, and S. Barman, "Competing tetragonal and monoclinic phases in $Ni_{2.2}Mn_{0.80}Ga$," *J. Appl. Phys.*, vol. 106, no. 3, p. 033510, 2009.

[60] P. Lotti, S. Milani, M. Merlini, B. Joseph, F. Alabarse, and A. Lausi, "Single-crystal diffraction at the high-pressure Indo-Italian beamline Xpress at Elettra, Trieste," *J. Synchrotron Radiat.*, vol. 27, no. 1, pp. 222–229, 2020.

[61] J. P. Perdew, K. Burke, and M. Ernzerhof, "Generalized Gradient Approximation Made Simple," *Phys. Rev. Lett.*, vol. 77, pp. 3865–3868, Oct 1996.

[62] P. Giannozzi, S. Baroni, N. Bonini, M. Calandra, R. Car, C. Cavazzoni, D. Ceresoli, G. L. Chiarotti, M. Cococcioni, I. Dabo, *et al.*, "QUANTUM ESPRESSO: a modular and open-source software project for quantum simulations of materials," *J. Condens. Matter Phys.*, vol. 21, no. 39, p. 395502, 2009.

[63] D. R. Hamann, "Optimized norm-conserving vanderbilt pseudopotentials," *Phys. Rev. B*, vol. 88, p. 085117, Aug 2013.

[64] K. Buschow and D. De Mooij, "Crystal structure and magnetic properties of PtMnGa and PtMnAl," *J. Less-Common Met.*, vol. 99, no. 1, pp. 125–130, 1984.

[65] A. K. Singh, S. Singh*, K. K. Dubey, P. Devi, P. Das, M. Etter, O. G. Grendal, C. Dejoie, A. Fitch, A. Senyshyn, S.-C. Lee, S. Bhattacharjee, and D. Pandey, "Evidence for Local Symmetry Breaking in the Skyrmion-Hosting Ni_2In-type Hexagonal Compounds." arXiv:2412.09158v1 [cond-mat.mtrl-sci].

[66] H. E. Stanley, *Phase transitions and critical phenomena*, vol. 7. Clarendon Press, Oxford, 1971.

[67] H. Nishimori and G. Ortiz, *Elements of phase transitions and critical phenomena*. Oxford university press, 2011.

[68] V. Rajaji, U. Dutta, P. Sreeparvathy, S. C. Sarma, Y. Sorb, B. Joseph, S. Sahoo, S. C. Peter, V. Kanchana, and C. Narayana, "Structural, vibrational, and electrical properties of 1 T$-$TiTe$_2$ under hydrostatic pressure: Experiments and theory," *Phys. Rev. B*, vol. 97, no. 8, p. 085107, 2018.

[69] G. Li, Y. Li, M. Zhang, Y. Ma, Y. Ma, Y. Han, and C. Gao, "Pressure-induced isostructural phase transition in CaB_4," *RSC Adv.*, vol. 4, no. 80, pp. 42523–42529, 2014.

[70] S. N. Gupta, A. Singh, S. Sarkar, D. Muthu, S. Sampath, U. Waghmare, and A. Sood, "Pressure-induced electronic and isostructural phase transitions in PdPS: Raman, x-ray, and first-principles study," *Phys. Rev. B*, vol. 101, no. 3, p. 035123, 2020.

[71] Q. Liu, X. Yu, X. Wang, Z. Deng, Y. Lv, J. Zhu, S. Zhang, H. Liu, W. Yang, L. Wang, *et al.*, "Pressure-Induced Isostructural Phase Transition and Correlation of FeAs Coordination with the Superconducting Properties of 111-type $Na_{(1-x)}FeAs$," *J. Am. Chem. Soc.*, vol. 133, no. 20, pp. 7892–7896, 2011.

[72] S. Karmakar, S. M. Sharma, P. Teredesai, and A. Sood, "Pressure-induced phase transitions in iron-filled carbon nanotubes: X-ray diffraction studies," *Phys. Rev. B*, vol. 69, no. 16, p. 165414, 2004.

[73] M. Mitrano, B. Maroni, C. Marini, M. Hanfland, B. Joseph, P. Postorino, and L. Malavasi, "Anisotropic compression in the high-pressure regime of pure and chromium-doped vanadium dioxide," *Phys. Rev. B*, vol. 85, no. 18, p. 184108, 2012.

[74] F. D. Murnaghan, "The compressibility of media under extreme pressures," *Proc. Natl. Acad. Sci.*, vol. 30, no. 9, pp. 244–247, 1944.

[75] F. Birch, "Finite elastic strain of cubic crystals," *Phys. Rev.*, vol. 71, no. 11, p. 809, 1947.

[76] F. Rivadulla, M. Bañobre-López, C. X. Quintela, A. Piñeiro, V. Pardo, D. Baldomir, M. A. López-Quintela, J. Rivas, C. A. Ramos, H. Salva, *et al.*, "Reduction of the bulk modulus at high pressure in CrN," *Nat. Mater.*, vol. 8, no. 12, pp. 947–951, 2009.

[77] B. Zhang, C. An, X. Chen, Y. Zhou, Y. Zhou, Y. Yuan, C. Chen, L. Zhang, X. Yang, and Z. Yang, "Structural and electrical transport properties of charge density wave material $LaAgSb_2$ under high pressure," *Chin. Phys. B*, vol. 30, no. 7, p. 076201, 2021.

[78] S. B. Pillai, B. Joseph, D. Upadhyay, C. Marini, and P. K. Jha, "Pressure Induced Hydrogen Order-Disorder Transition in β-$Ni(OH)_2$," *J. Phys. Chem. C*, vol. 125, no. 4, pp. 2785–2792, 2021.

[79] R. Vilaplana, D. Santamaría-Pérez, O. Gomis, F. Manjón, J. González, A. Segura, A. Muñoz, P. Rodríguez-Hernández, E. Pérez-González, V. Marín-Borrás, *et al.*, "Structural and vibrational study of Bi_2Se_3 under high pressure," *Phys. Rev. B*, vol. 84, no. 18, p. 184110, 2011.

[80] A. Polian, M. Gauthier, S. M. Souza, D. M. Trichês, J. C. de Lima, and T. A. Grandi, "Two-dimensional pressure-induced electronic topological transition in Bi_2Te_3," *Phys. Rev. B*, vol. 83, no. 11, p. 113106, 2011.

[81] E. Chason and P. R. Guduru, "Tutorial: Understanding residual stress in polycrystalline thin films through real-time measurements and physical models," *J. Appl. Phys.*, vol. 119, no. 19, 2016.

[82] C. E. Murray and K. Saenger, "Mechanical behavior of stressed films on anisotropic substrates," *J. Appl. Phys.*, vol. 104, no. 10, 2008.

[83] E. Chason, B. Sheldon, L. Freund, J. Floro, and S. Hearne, "Origin of compres-

sive residual stress in polycrystalline thin films," *Phys. Rev. Lett.*, vol. 88, no. 15, p. 156103, 2002.

[84] W. Jayasekara, U. Kaluarachchi, B. Ueland, A. Pandey, Y. Lee, V. Taufour, A. Sapkota, K. Kothapalli, N. Sangeetha, G. Fabbris, *et al.*, "Pressure-induced collapsed-tetragonal phase in $SrCo_2As_2$," *Phys. Rev. B*, vol. 92, no. 22, p. 224103, 2015.

[85] S. Shen, S. Feng, Z. Lin, Z. Wang, and W. Zhong, "Ferromagnetic behavior induced by La-doping in $SrCo_2As_2$," *J. Mater. Chem. C*, vol. 6, no. 30, pp. 8076–8081, 2018.

[86] W. Wang, Y. Zhang, G. Xu, L. Peng, B. Ding, Y. Wang, Z. Hou, X. Zhang, X. Li, E. Liu, S. Wang, J. Cai, F. Wang, J. Li, F. Hu, G. Wu, B. Shen, and X.-X. Zhang, "A Centrosymmetric Hexagonal Magnet with Superstable Biskyrmion Magnetic Nanodomains in a Wide Temperature Range of 100–340 K," *Adv. Mater.*, vol. 28, no. 32, pp. 6887–6893, 2016.

[87] L. Bo, X. Zhang, M. Mochizuki, and X. Zhang, "Suppression of the skyrmion Hall effect in synthetic ferrimagnets with gradient magnetization," *Phys. Rev. Res.*, vol. 6, no. 2, p. 023199, 2024.

[88] Y. Zhang, S. Luo, B. Yan, J. Ou-Yang, X. Yang, S. Chen, B. Zhu, and L. You, "Magnetic skyrmions without the skyrmion Hall effect in a magnetic nanotrack with perpendicular anisotropy," *Nanoscale*, vol. 9, no. 29, pp. 10212–10218, 2017.

[89] M. J. Donahue and D. G. Porter, "OOMMF user's guide, version 1.0," 1999.

[90] G. Hadjipanayis, D. J. Sellmyer, and B. Brandt, "Rare-earth-rich metallic glasses. I. magnetic hysteresis," *Phys. Rev. B*, vol. 23, no. 7, p. 3349, 1981.

[91] A. Franco, H. Pessoni, and F. Machado, "Spin-wave stiffness parameter in ferrimagnetic systems: Nanoparticulate powders of (Mg, Zn) Fe_2O_4 mixed ferrites," *J. Appl. Phys.*, vol. 118, no. 17, 2015.

[92] R. Y. Umetsu and T. Kanomata, "Spin stiffness constant of half-metallic ferrimagnet in Mn-based Heusler alloys," *Phys. Procedia*, vol. 75, pp. 890–897, 2015.

[93] T. L. Gilbert, "A phenomenological theory of damping in ferromagnetic materials," *IEEE Trans. Magn.*, vol. 40, no. 6, pp. 3443–3449, 2004.

[94] X. Zhang, J. Xia, Y. Zhou, X. Liu, H. Zhang, and M. Ezawa, "Skyrmion dynamics in a frustrated ferromagnetic film and current-induced helicity locking-unlocking transition," *Nat. Commun.*, vol. 8, no. 1, p. 1717, 2017.

[95] X. Zhang, G. Zhao, H. Fangohr, J. P. Liu, W. Xia, J. Xia, and F. Morvan, "Skyrmion-skyrmion and skyrmion-edge repulsions in skyrmion-based racetrack memory," *Sci. Rep.*, vol. 5, no. 1, p. 7643, 2015.

[96] J. E. Miltat, M. J. Donahue, *et al.*, "Numerical micromagnetics: Finite difference methods," *Handb. Magn. and Adv. Magn. Mater.*, vol. 2, pp. 742–764, 2007.

[97] W. Brown, "Micromagnetics, Interscience Publisher," *Interscience Publisher, New York, London*, 1963.

[98] R. Li, S. Zhang, S. Luo, Z. Guo, Y. Xu, J. Ouyang, M. Song, Q. Zou, L. Xi, X. Yang, *et al.*, "A spin–orbit torque device for sensing three-dimensional magnetic fields," *Nat. Electron.*, vol. 4, no. 3, pp. 179–184, 2021.

[99] H. Wu, X. Hu, K. Jing, and X. Wang, "Size and profile of skyrmions in skyrmion crystals," *Commun. Phys.*, vol. 4, no. 1, p. 210, 2021.

[100] S. Rohart and A. Thiaville, "Skyrmion confinement in ultrathin film nanostructures in the presence of Dzyaloshinskii–Moriya interaction," *Phys. Rev. B*, vol. 88, no. 18, p. 184422, 2013.

[101] S. Rastogi, N. Shahi, V. Kumar, G. K. Shukla, S. Bhattacharjee, and S. Singh, "Revealing the origin of the topological Hall effect in the centrosymmetric shape memory Heusler alloy Mn_2NiGa: A combined experimental and theoretical investigation," *Phys. Rev. B*, vol. 108, no. 22, p. 224108, 2023.

[102] A. Michels, D. Mettus, I. Titov, A. Malyeyev, M. Bersweiler, P. Bender, I. Peral, R. Birringer, Y. Quan, P. Hautle, *et al.*, "Microstructural-defect-induced Dzyaloshinskii–Moriya interaction," *Phys. Rev. B*, vol. 99, no. 1, p. 014416, 2019.

[103] D. Cortés-Ortuño, "OMMF Skyrmion Number (v0.1), Zenodo.," *https://doi.org/10.5281/zenodo.1296536*, 2018.

[104] X. Zhang, J. Xia, Y. Zhou, D. Wang, X. Liu, W. Zhao, and M. Ezawa, "Control and manipulation of a magnetic skyrmionium in nanostructures," *Phys. Rev. B*, vol. 94, no. 9, p. 094420, 2016.

[105] F. Morvan, H. Luo, H. Yang, X. Zhang, Y. Zhou, G. Zhao, W. Xia, and J. Liu, "An achiral ferromagnetic/chiral antiferromagnetic bilayer system leading to controllable size and density of skyrmions," *Sci. Rep.*, vol. 9, no. 1, p. 2970, 2019.